

Chapter

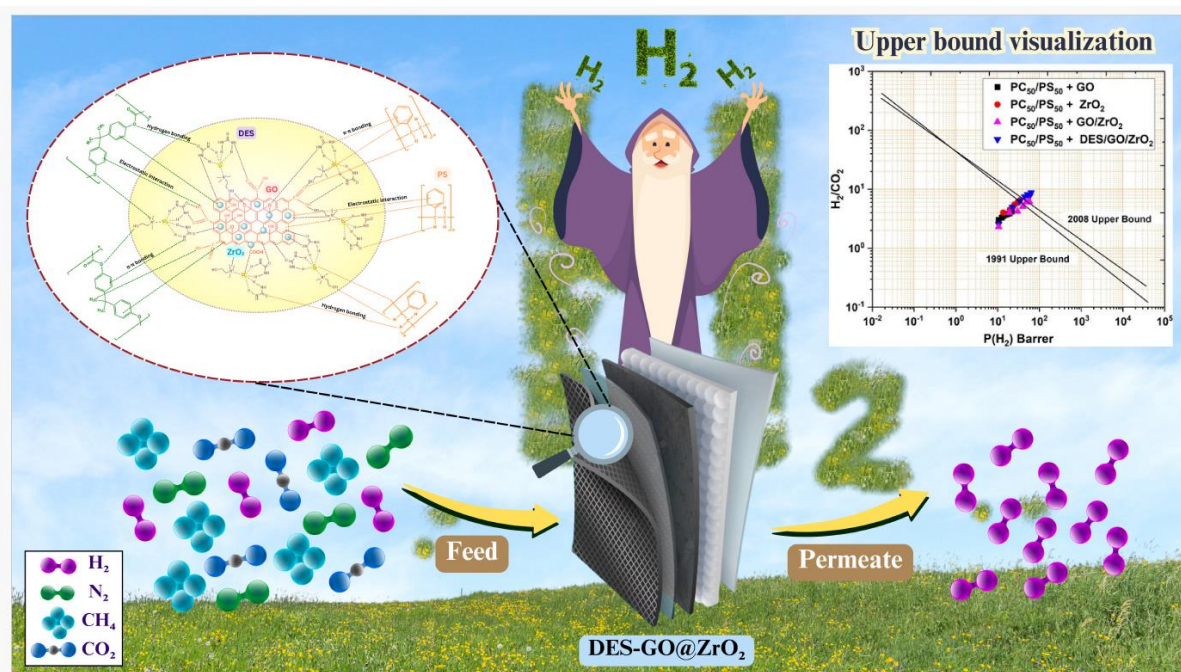
6

A Polymer blend NCs for the separation and purification of gases

Contents

- 6.1** Introduction
- 6.2** Experimental section
- 6.3** Result and discussion
 - 6.3.1** FTIR Analysis
 - 6.3.2** XRD Analysis
 - 6.3.3** SEM-EDX analysis
 - 6.3.4** Thermal Properties
 - 6.3.5** Contact Angle Analysis
 - 6.3.6** Thickness and Porosity Measurements
 - 6.3.7** Mechanical Properties
 - 6.3.8** Gas permeability
 - 6.3.9** Selectivity and upper bound visualization
- 6.4** Conclusion

In this Chapter, Mixed matrix membrane (MMM) based gas separation technologies has been introduced. This chapter focuses on the membrane fabrication and characterization of various blend-composites with and without DESs. MMMs are fabricated (cost and time effective standard phase inversion technique) by blending PC and PS together with GO and ZrO_2 as nanofillers. The fabricated MMMs were characterized using other characterization techniques such as DSC, TGA, SEM, XRD, porosity determination wet-dry method, and contact angle. The gas permeability measurement with fabricated MMMs was accomplished by a constant pressure/ variable volume system using a bubble flowmeter.



6.1 Introduction

In the future, global energy consumption is expected to escalate. Hence, it is desirable to exploit and invent new and efficient energy sources [1]. The energy derived from the combustion of fossil fuels, especially for industrial consumption and transportation, results in the emission of greenhouse gases and environmental pollution. Therefore, as a remedy, multifarious fuels such as methanol, ethanol, methane gas, and hydrogen derived from clean energy sources are explored [2,3]. Furthermore, renewable resources have already gained substantial importance in the global energy portfolio. The demand for pure hydrogen is increasing and the current production of hydrogen reaches 95 million tonnes per year globally [4]. The majority of hydrogen production is derived from the methane steam reforming process, whereas the rest is generated

from coal [5]. Fossil fuels serve as the primary source of hydrogen for various chemical industries, making it a vital component in modern industrial processes. Hydrogen has significant applications in oil refineries, ammonia/methanol production, metal-based fabrications, food processing, electronics, energy storage and fuel cells [6–10]. Hydrogen is also extensively utilized across various sectors, including hydrotreating biofuels and enhancing the quality of oil sands [11,12]. Potentially, hydrogen is going to be the next-generation energy source to solve the global warming problem and, therefore, it is crucial to address the challenges associated with pure hydrogen production and its storage [2,3]. Clean hydrogen can be generated through a diverse range of domestic energy sources, encompassing nuclear energy, coal gasification, natural gas, and renewable energy sources (solar, geothermal, biomass, wind, hydroelectric, and ocean thermal energy conversion) [13–15]. Multiple technologies are available for the separation and purification of hydrogen such as wet scrubbing, dry scrubbing, cryogenic distillation, membrane separation, and pressure swing adsorption [16,17]. Out of these, membrane separation technology has gained significant momentum due to its operational flexibility, compactness, energy efficiency, simplicity, environmental friendliness, and low operating cost [18].

In general, membrane performance depends on the nature of the membrane material, its interaction with the gas, physicochemical properties, thickness, and gas transport variables [19]. The advancement of hydrogen-selective membranes involves the utilization of various materials, including glassy polymer membranes (polyimide, polystyrene, polycarbonate, polysulfone, etc.), inorganic membranes (TiO_2 , zeolite, silica, and metal oxides) and metallic membranes (Pd or Pt) [20–22]. Polymer membrane offers excellent mechanical strength, versatility for different module configurations, cost-effectiveness, and reproducibility [23]. However, the progress of polymeric membrane separation processes has been hindered by the consistency of the ‘upper bound’ trade-off relationship (Robeson’s plot), which relates gas permeability with selectivity [24,25]. To meet industrial requirements, membrane performance must be improved in terms of selectivity and permeability. This improvement can be achieved by integrating membrane material with manufacturing technologies. Glassy polymers have emerged as promising materials for gas separation due to their notable gas selectivity and robust mechanical strength. Such membranes are particularly suitable for separating small-sized gas molecules like H_2 , which have higher permeability compared to larger-sized molecules such as CO_2 and N_2 [19,26]. Among these, polycarbonate (PC) and polystyrene (PS) membranes bring distinct advantages in gas separation applications. PC membranes exhibit good mechanical properties and withstand under extreme conditions. H_2 shows higher permeability than CO_2 through PC membranes, potentially due to molecular shape differences. Etching PC membranes enhances permeability and selectivity [27].

Recently, Acharya et al. [28] revealed that the permeability of H₂ is higher than that of CO₂ when passing through a PC (specifically bisphenol-A polycarbonate) membrane. Furthermore, PS membranes excel in gas separation because of their molecular properties and increased durability, chemical resistance, and thermal stability [29].

In recent times, technologies have been developed based on new generation of membrane matrix, composed of inorganic filler within an organic framework, serving as future materials for gas separation. The loading of nano-fillers within the polymer matrix membrane promotes gas transport properties and also influences the separation factor up to a certain extent [30,31]. Extensive research is underway on porous graphene and GO NC membranes for gas separation [32–34]. GO exhibits a hexagonal pattern and contains functional oxygen groups on its surface [35], enabling versatile interactions with other molecules via sp² hybridization and π-π interactions [36,37]. In addition, GO dissolves easily in water and other solvents because of the presence of oxygen functional groups [38]. Porous inorganic ceramic membranes, including materials such as Al₂O₃, SiO₂, TiO₂, and ZrO₂, either individually or in combination, hold great potential for gas permeation and liquid separation at elevated temperatures in aggressive environments where commercial polymer membranes pose limitations [39–41]. Zirconia exhibits increased chemical stability compared with gamma alumina and titania, making it suitable for applications requiring gas and liquid separation at elevated temperatures (with alkali durability and stability) [42–44].

As discussed in previous chapters, DESs have emerged as a superior substitute of ILs with improved properties. Reline can be obtained by mixing of ChCl and urea in a fixed molar ratio (ChCl: urea, 1:2) [45–47]. DES supported membranes have gained significant momentum in various research fields including biotechnology, bioengineering, food industry, environmental purification, biomass pre-treatment and conversion, recovery processes and solvent-gas separation [48–55]. Most recently, DES-functionalized GO membranes for gas separation have demonstrated high selectivity for CO₂ separation [56]. The combination of DES with high-porosity membranes has emerged as an attractive feature, leading to the development of next-generation mixed matrix membranes (MMMs) capable of meeting real-world demands [57]. However, DES modified GO-metal oxide nanofillers are not applied to fabricate MMMs. DES modifies polymer membranes to enhance gas permeability and selectivity by creating a unique solvent environment that optimizes membrane morphology and facilitates gaseous diffusion. The integration of inorganic nanoparticles in MMMs and the utilization of DES as a modifier can play a crucial role in pure hydrogen production and in advancing clean energy technologies.

In this chapter, the blending of PC and PS was accomplished using a simple phase-inversion technique [58]. Both glassy polymers are used in equal amounts (50 wt% each). The nanofillers (GO, ZrO₂, GO/ZrO₂ and DES/GO-ZrO₂) were used in different amounts (2 wt% to 20 wt%). The gas permeability measurement with fabricated MMMs was accomplished by a constant pressure/ variable volume system using a bubble flowmeter [59]. Moreover, the separation factor was computed using a single gas permeability parameter, which is further evaluated for the trade of upper bound for H₂ gas. The MMMs were thoroughly characterized before use (by spectroscopic, thermal, morphological and mechanical techniques).

6.2 Experimental section

The materials and methods used are discussed in chapter 2.

6.3 Result and discussion

6.3.1 FTIR

The FTIR spectra of pure NCs are discussed in chapter 3. The modification of PNCs has been further confirmed by FTIR spectroscopy [Figure 6.1](#).

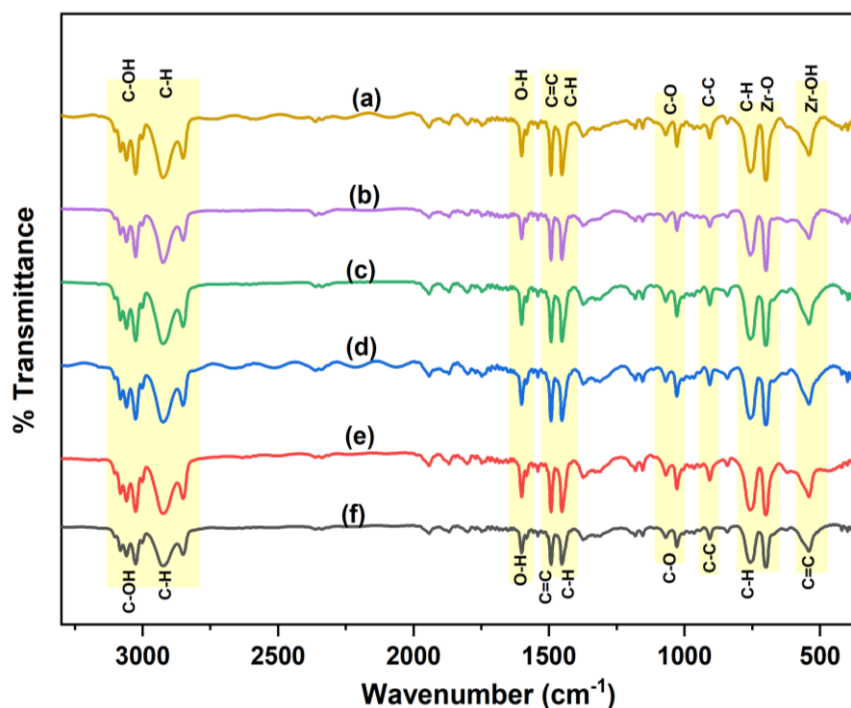
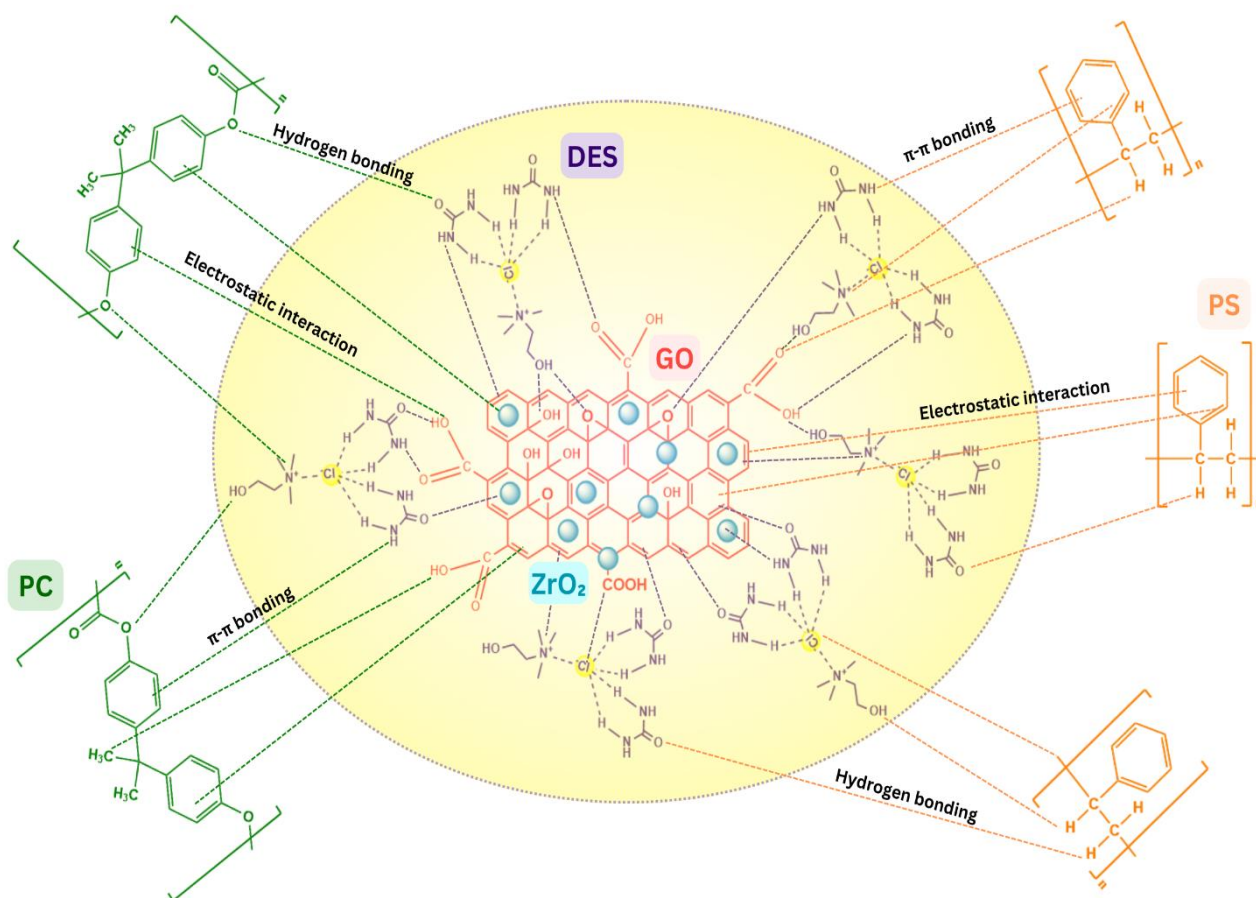


Figure 6.1: FTIR spectra of polymer blend composites (a) PC₅₀/PS₅₀+ 20 wt% DES-GO/ZrO₂ (b) PC₅₀/PS₅₀+ 5 wt% DES-GO/ZrO₂ (c) PC₅₀/PS₅₀+ 20 wt% GO/ZrO₂ (d) PC₅₀/PS₅₀+ 5 wt% GO/ZrO₂ (e) PC₅₀/PS₅₀+ 20 wt% ZrO₂ (f) PC₅₀/PS₅₀+ 20 wt% GO.

The band at 3224 cm^{-1} in the FTIR spectra indicates the O-H stretching vibrations of hydroxyl groups (**Figure 6.1**). Additionally, the bands at 1046 cm^{-1} , 3110 cm^{-1} , 973 cm^{-1} , and 1121 cm^{-1} represent C-O and C-OH stretching vibrations, C-C vibrations from sp_2 graphitic domains, and C-O stretching vibrations of carboxylic acid groups, respectively. The FTIR spectrum of DES-GO/ZrO₂ blend composites shows characteristic bands at 712 cm^{-1} (Zr-O stretching), 792 cm^{-1} (C-H symmetric stretching), 953 cm^{-1} (C-C symmetric stretching), 1036 cm^{-1} , and 1045 cm^{-1} (asymmetric and symmetric stretching of C-O), and 1039 cm^{-1} (C-C). **Scheme 6.1** represents a possible interaction between NCs with a polymer blend of PC and PS, including hydrogen bonding, π - π bonding, and electrostatic interaction. All MMMs showed a large peak at 3117 cm^{-1} that was caused by the O-H stretching vibration of hydroxyl groups. As seen in **Figure 6.1**, GO/ZrO₂ shared the same infrared characteristic peaks with DES-GO/ZrO₂. These peaks correspond to the symmetric and asymmetric stretching vibrations of C-H on Zr-O and C-OH, the stretching vibration of C=C on the benzene ring, and the bending vibration of O-H in GO/ZrO₂, respectively. The peak at 720 cm^{-1} and 838 cm^{-1} (Zr-O stretching vibrations) have maxima in the FTIR spectra of ZrO₂ and the O-H bending vibration of water molecules at 1603 cm^{-1} , 3031 cm^{-1} , and 3345 cm^{-1} , respectively. The O-H stretching vibration peak is located at 3345 cm^{-1} , the C=C stretching vibration peak is located at 1492 cm^{-1} , the Zr-O-Zr stretching vibration peak is located at 1345 cm^{-1} , and the C-O skeleton stretching vibration peak is located at 1219 cm^{-1} , respectively, in the spectrum of GO/ZrO₂. It confirms that GO and ZrO₂ were effectively combined in the nanohybrid [60,61].

Although there are significant peak shifts, the peaks in the FTIR spectra of DES-GO/ZrO₂ and GO/ZrO₂ nanofillers mainly resemble those of GO/ZrO₂. This suggests that the GO/ZrO₂ fillers have been effectively functionalized by DES. The FTIR spectrum of DES-GO/ZrO₂ changed after the reaction, revealing a peak at 1495 cm^{-1} attributed to C=C and several minor bands around 2919 cm^{-1} and 1442 cm^{-1} , which are attributed to the C-H stretching vibrations of the hydrocarbon chains. These changes indicate that the GO fillers were successfully grafted onto the surface of ZrO₂. Specifically, the characteristic peaks in the FTIR of PC₅₀/PS₅₀+ 20 wt% DES-GO/ZrO₂ samples include peaks at 3110 cm^{-1} (C-OH), 2951 cm^{-1} (symmetric stretching of C-H), 1603 cm^{-1} (O-H stretching), 1492 cm^{-1} (C=C stretching), 1442 cm^{-1} (C-H bending), 1025 cm^{-1} (C-O), 906 cm^{-1} (C-C bending), 752 cm^{-1} (C-H), 695 cm^{-1} and 538 cm^{-1} corresponding to Zr-O and Zr-OH stretching. In the case of PC₅₀/PS₅₀+ 5 wt% DES-GO/ZrO₂, whereas the C-O stretching bands from carboxylic acid groups only slightly changed from 1725 cm^{-1} to 1706 cm^{-1} . The O-H stretching vibration for the GO, which was previously at 1603 cm^{-1} , was similarly decreased and shifted to 1603 and 1596 cm^{-1} for PC₅₀/PS₅₀+ 20 wt% DES-GO/ZrO₂. As a result

of partial reduction by PC₅₀/PS₅₀+ 5 wt% DES-GO/ZrO₂ functionalization and replacement by nitrogen-containing functional groups with the corresponding bands described above, the C-O and O-H bands in the DES-GO/ZrO₂ nanofillers have shifted [62].



Scheme 6.1: Schematics illustration of the possible interaction between NCs and polymer blend of PC and PS.

6.3.2 XRD

XRD spectra of pure NCs are discussed in chapter 3. The XRD spectra of the blend of PC₅₀/PS₅₀, PC₅₀/PS₅₀ + GO, PC₅₀/PS₅₀ + GO/ZrO₂ and PC₅₀/PS₅₀ + DES-GO/ZrO₂ membrane films are shown in **Figure 6.2**. The results show that the GO, ZrO₂, GO/ZrO₂ and DES-GO/ZrO₂ hybrid nanofillers could be dispersed uniformly in the blend composites matrix of PC₅₀/PS₅₀, transforming the amorphous structure into the semi-crystalline structure in the blend composites membranes [63,64]. A significant diffraction peak for the PC₅₀/PS₅₀ + GO sample can be seen at $2\theta = 20.75^\circ$, corresponding to an interlayer spacing of 7.23 Å. The interlayer spacing decreased to 6.74 Å after functionalization with DES-GO/ZrO₂, as seen by the shift of the GO suggestive peak in the DES-GO/ZrO₂ sample to $2\theta = 19.93^\circ$. According to earlier research, the action of additional functional groups given to the GO during functionalization with DES-

GO/ZrO₂ may be responsible for this decrease in the interlayer gap between DES-GO/ZrO₂ nanofillers. Additionally, the carbon peak in the DES-GO/ZrO₂ has broadened at $2\theta = 19.93^\circ$, indicating a partial reduction of the GO due to the restoration of sp² domains after DES functionalization. In the XRD spectra of the DES-GO/ZrO₂ sample, the broadened peak becomes narrower and sharper after the functionalization with DES, forming a single noticeable broad peak at $2\theta = 20.23^\circ$ for the sample of PC₅₀/PS₅₀ + 5 wt% DES-GO/ZrO₂. This characterizes additional gradual reduction and replacement of oxygen functional groups in the GO nanosheets [59]. This broadened DES-GO/ZrO₂ peak also indicates the presence of defects and surface wrinkles, as well as the fact that enhanced DES functionalization results in more stacked and semi-crystalline graphene sheets. After blend composite of GO/ZrO₂ and DES-GO/ZrO₂, the interlayer spacing of the GO/ZrO₂ and DES-GO/ZrO₂ membranes increased slightly, from 7.83 Å to 8.48 Å and from 8.10 Å to 8.93 Å, respectively. However, the increase in interlayer spacing of these membranes after composite formation with GO/ZrO₂ is substantially less than that shown in prior research when GO and ZrO₂ membranes expanded due to the presence of DES solvent. These stacked and wrinkled DES-GO/ZrO₂ nanofillers may facilitate the transport of gas molecules when used as membranes with a PC₅₀/PS₅₀ polymer blend.

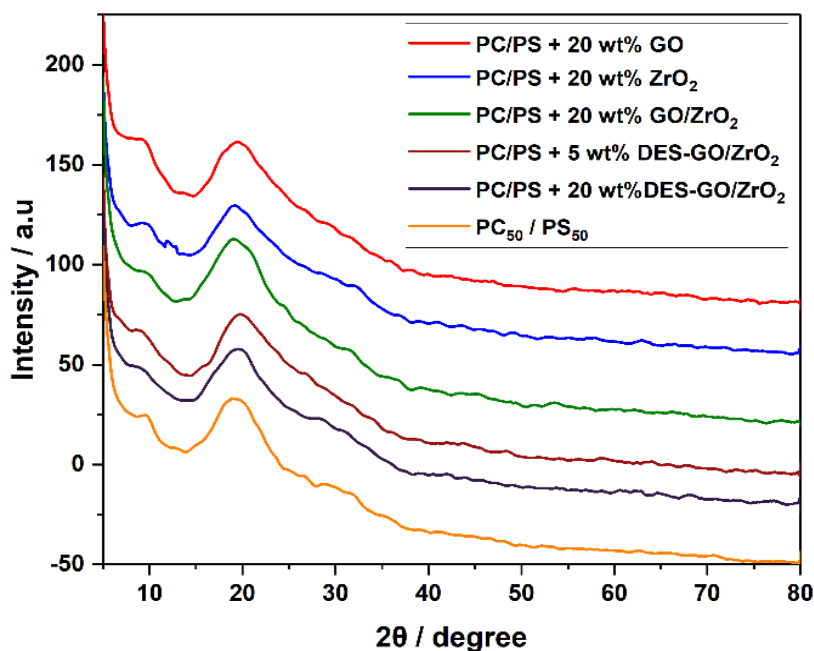


Figure 6.2: XRD patterns of polymer blend composites (MMMs).

6.3.3. SEM-EDX

To see the morphological properties of the NCs, SEM-EDX analysis was performed on all the developed membranes. The elemental analysis data are summarized in the **Table 6.1**. EDX elemental maps show the presence of carbon (C), oxygen (O), zirconium (Zr), nitrogen (N), and

chlorine (Cl) in the NCs (**Figure 6.3 (a-b)**). This indicates that the GO nanosheets and ZrO₂ nanoparticles have been effectively linked through surface modification of GO using

DES [65]. SEM images of NCs show the presence of more aggregated graphene structures coated with ZrO₂ nanoparticles scattered throughout and covering a significant portion of the surface. The dispersion of GO/ZrO₂, DES-GO/ZrO₂ hybrid composites membranes at the nanometric scale was further confirmed by SEM images. Additionally, particle agglomeration at the polymer filler interface was observed, as shown in **Figure 6.3 (a-f)**, with several dense bundles of GO/ZrO₂ seen in the hybrid samples. It is important to note that the van der Waals forces between the GO and ZrO₂ promote this agglomeration. As a result, composites with DES-GO/ZrO₂ exhibited an increased tendency for agglomeration. The average size and form of all GO/ZrO₂, DES-GO/ZrO₂ nanofillers as well as the morphology of the resulting membrane, were studied using SEM. The picture clearly shows several large-sized agglomerated nanoparticles in addition to GO/ZrO₂, and DES-GO/ZrO₂ nanofillers. **Figure 6.3 (c-f)** presents a smooth surface appearance representing a thick blended composite polymer membrane. Due to the inclusion of DES during the making of the membrane, the EDX test shows a minor intensity peak of N and Cl in the DES-GO/ZrO₂ composite membrane (**Figure 6.3 (b)**).

Table 6.1: EDX elemental analysis of GO/ZrO₂ and DES-GO/ZrO₂

Elements	GO/ZrO ₂		DES-GO/ZrO ₂	
	Weight %	Atomic %	Weight %	Atomic %
C	42.43	60.75	52.48	68.22
O	30.22	33.94	23.52	26.30
Zr	27.35	5.31	22.75	4.48
N	-	-	0.96	0.58
Cl	-	-	0.29	0.42

Some larger particles result from the aggregation or overlap of smaller particles. SEM images clearly depict randomly distributed, smaller-sized grains with a uniform spherical shape. Quantitative analysis validated the synthesis and composition of crystalline ZrO₂ nanoparticles, indicating that the sample exclusively contains Zr and O, confirming its high purity without any impurities. To examine the impact of DES functionalization on the elemental composition of DES-GO/ZrO₂ membranes, EDX analysis was conducted in conjunction with SEM imaging (**Figure 6.3 (a-b)**). The oxygen content decreased from 30.22% in GO/ZrO₂ to 23.52% in DES-GO/ZrO₂, confirming the partial and progressive reduction of GO by DES. Additionally, the

carbon content increased from 42.53% in GO/ZrO₂ to 52.48% in DES-GO/ZrO₂, providing evidence of increased graphitization due to DES. Furthermore, zirconium content decreased from 27.35% in GO/ZrO₂ to 22.75% in DES-GO/ZrO₂, attributed to the overlapping of GO nanosheets with ZrO₂ nanofillers due to the DES solvent (Table 6.1). The DES-GO/ZrO₂ nanofillers were evenly deposited on the PC₅₀/PS₅₀ surface using the phase inversion method, as their lateral size exceeded that of the GO, ZrO₂, and GO/ZrO₂ pore size. The surfaces of ZrO₂ (Figure 6.3 (c)), GO (Figure 6.3 (d)) and GO/ZrO₂ (Figure 6.3 (e)) membranes appear smoother than those of DES-GO/ZrO₂ membranes, as shown in Figure 6.3 (f). The SEM image of these membranes reveals the DES-GO/ZrO₂ composite membrane, which consists of a thin active layer of GO and ZrO₂ with a thickness of approximately ~85 μm atop the polymeric substrate layer, featuring several microvoids within.

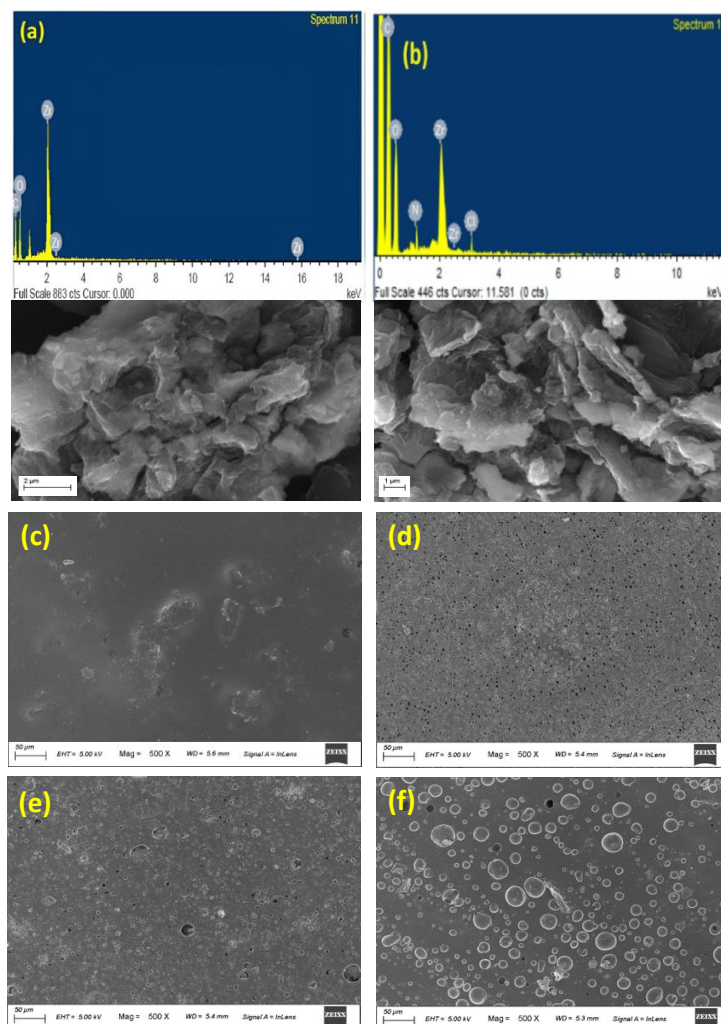


Figure 6.3: SEM-EDX analysis of (a) GO/ZrO₂, (b) DES-GO/ZrO₂ (c) PC₅₀/PS₅₀+ 20 wt% ZrO₂ (d) PC₅₀/PS₅₀+ 20 wt% GO (e) PC₅₀/PS₅₀+ 20 wt% GO/ZrO₂ (f) PC₅₀/PS₅₀+ 20 wt% DES-GO/ZrO₂

6.3.4 Thermal Properties

Figure 6.4 shows the DSC thermal analysis of PC₅₀/PS₅₀ blends with different nanofillers like GO and ZrO₂ with different weight ratios. The glass transition temperatures (T_g) of the blend composites have been determined to range from 97.55°C to 98.98°C. The DSC curve is used to determine the glass transition temperatures (T_g) of each blend composite sample. Each sample under study has a curve that corresponds to the glass transition temperatures (T_g) of the blend composites membranes [66]. The reason why the glass transition temperature increased when we composite with ZrO₂, is due to the high melting temperature of ZrO₂, it is possible to notice a considerable increase in the melting temperature for PC₅₀/PS₅₀ blend composites membranes. This property can be explained by the role of ZrO₂ and GO nanosheets during the synthesis of PNCs as nano-compatible. As expected, the glass transition temperature of the PC₅₀/PS₅₀+ 20 wt% ZrO₂ membrane is much greater than that of other composite membranes and also greater than PC₅₀/PS₅₀ blend membrane [67]. This is because ZrO₂ has a monoclinic structure; as a result, more energy is required to break the interchain interactions between molecules of ZrO₂. According to earlier research, the better thermal stability of PC₅₀/PS₅₀+ 20 wt% GO/ZrO₂ is due to the homogenous dispersion of ZrO₂ and GO with the blend's polymers. The glass transition temperature of PC₅₀/PS₅₀+ 20 wt% ZrO₂ is 98.98 °C greater than that of PC₅₀/PS₅₀+ 20 wt% GO/ZrO₂. This suggests that the majority of GO fillers were doped by ZrO₂ nanosheets due to their aggregation in the PC₅₀/PS₅₀ blend, and as a result, the glass transition temperature of PC₅₀/PS₅₀+ 20 wt% GO/ZrO₂ is lower as compared to PC₅₀/PS₅₀+ 20 wt% ZrO₂. This observation offered us another very strong evidence that the composite ZrO₂ played a crucial role in the uniform distribution of GO/ZrO₂ in polymer blends of PNCs. The DSC analysis results show that the GO/ZrO₂ are amorphous and that the T_g increases within the polymer blend of PC₅₀/PS₅₀. On the other hand, since the ZrO₂ nanofillers enhance the stiffness of the polymer chain of PC₅₀/PS₅₀, and the T_g values gradually increase when ZrO₂ content is increased [68].

The thermal stability of the pure NCs is discussed in chapter 3. TGA and derivative thermogravimetry (DTG) of these blend composite films are shown in **Figure 6.5 (i) and (ii)**. The temperature of weight losses of 5%, 50%, 95%, and T_{max} . The char yield (%) at 500 °C has been studied to determine the impact of composite addition on the thermal stability of PC₅₀/PS₅₀ blends. **Table 6.2** shows different steps of temperatures of weight loss steps for all composites at 0 - 345 °C (5%), 345-364 °C (50%), 364-400 °C (95%) and 400-423 °C is the maximum temperature for weight loss. Decomposition of oxygen-containing groups existed on the GO surface (i.e., hydroxyl, carboxylic, and epoxide groups) and decomposition of the carbon skeleton of GO [69]. When compared to all the composites temperatures at which 50 % of weight loss has

occurred ($T_{50\%}$), the PC₅₀/PS₅₀+ 20 wt% GO composites have maximum weight loss and PC₅₀/PS₅₀+ 20 wt% ZrO₂ have minimum weight loss as compared to all other composites. According to the results, the composites of DES-GO/ZrO₂ nanofillers considerably improved their thermal stability. The PC₅₀/PS₅₀ nanocomposite blend films with a greater concentration of 20 wt% DES-GO/ZrO₂ nanosheets had lost less weight when compared to the GO/ZrO₂ and GO nanocomposite films, indicating that the DES-GO/ZrO₂ nanosheets significantly improve the heat stability of the PC₅₀/PS₅₀+DES-GO/ZrO₂ nanocomposite blend films. Several mechanisms have been proposed to explain this phenomenon: The flow of degradation product may be reduced by scattered nanofillers, polymer chains adjacent to nanotubes degrade more slowly and the onset of degradation is delayed, and nanofillers/polymer composites with superior thermal conductivity can dissipate heat more effectively [70]. The reason PC₅₀/PS₅₀+ 20 wt% ZrO₂ blends lose the minimum weight loss (~20%) is that ZrO₂ has a metallic nature and it has good thermal stability.

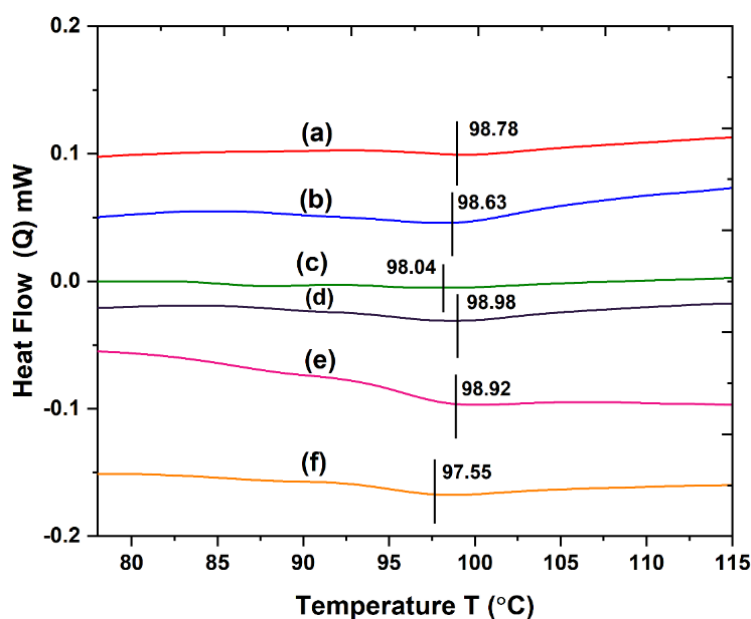


Figure 6.4: DSC analysis of (a) PC₅₀/PS₅₀+ 20 wt% DES-GO/ZrO₂ (b) PC₅₀/PS₅₀+ 20 wt% GO/ZrO₂ (c) PC₅₀/PS₅₀+ 20 wt% GO (d) PC₅₀/PS₅₀+ 20 wt% ZrO₂ (e) PC₅₀/PS₅₀+ 5 wt% ZrO₂ (f) PC₅₀/PS₅₀

To measure the thermal stability of the developed membranes, decomposition temperature (T_d) was used. T_d max. values have been determined to be 403.51 °C to 423.52 °C, for blend composites membranes. As a result, the thermal stability of PC₅₀/PS₅₀ blend membranes could certainly be improved by the suitable addition of ZrO₂ fillers [71]. The results show that the fictionalized GO/ZrO₂ nanosheets with DES cause nanocomposites blends of PC₅₀/PS₅₀+ DES-

GO/ZrO₂ show less weight loss and give better thermal stability than blends of PC₅₀/PS₅₀ and blends composites of PC₅₀/PS₅₀+ GO and PC₅₀/PS₅₀+ GO/ZrO₂. The DES-GO/ZrO₂ composites in the current study are thermally stable up to 418 °C, and it was the greatest percentage among the other composites like GO and GO/ZrO₂. The DES-GO/ZrO₂ nanosheets composite with PC₅₀/PS₅₀ blend show greater results in improving membrane thermal stability. The results indicate that the temperature of maximal thermal deterioration decreases with an increasing amount of DES-GO/ZrO₂ nanosheets after the functionalization of DES. The value of char yield (%) at 500 °C for 20 wt% of GO is 1.3%, GO/ZrO₂ (20 wt%) is 7.8%, DES-GO/ZrO₂ (20 wt%) is 11.6% and ZrO₂ (20 wt%) is 18.6%. As a result, the addition of DES-GO/ZrO₂ nanosheets slows the weight rate and improves the blends' thermal stability, producing a high char yield at higher temperatures. However, the thermal stability of these NCs did not show significant improvement in the case of GO/ZrO₂. The DES-GO/ZrO₂ composites PC₅₀/PS₅₀ blend's relative thermal stability was consistent with its physico-mechanical characteristics. The increased degree of cross-linkage and crystallinity of the matrix material may cause the composites' improved heat stability [72].

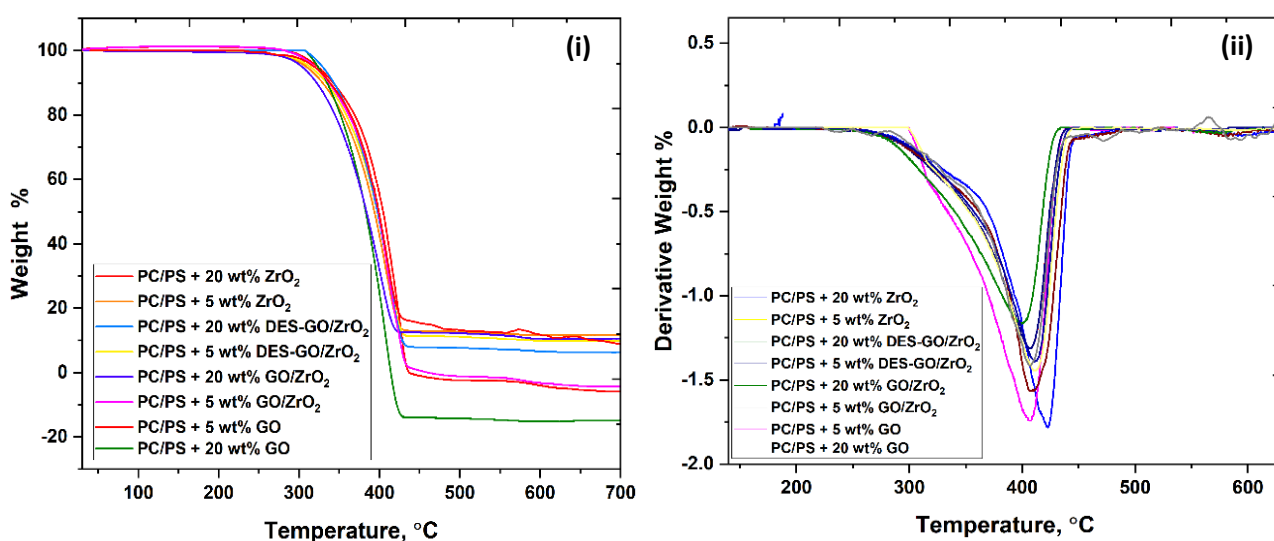


Figure 6.5: TGA analysis of (i) polymer blend composite films and (ii) DTG curve of polymer blend composite films.

Table 6.2: Thermal property of polymer blend nanocomposite of PC/PS composite with GO, ZrO₂, GO/ZrO₂ and DES-GO/ZrO₂ nanofillers.

Polymer Blends	Temperature at 5%, 50%, 95% and max. of weight loss				Char yield (%) 500 °C
	T _{5%} (°C)	T _{50%} (°C)	T _{95%} (°C)	T _{max} (°C)	
PC ₅₀ /PS ₅₀ + 5 wt% GO	320.95	343.52	386.54	403.51	0.6
PC ₅₀ /PS ₅₀ + 20 wt% GO	322.62	344.62	388.14	405.62	1.3
PC ₅₀ /PS ₅₀ + 5 wt% GO/ZrO ₂	328.63	346.45	389.26	409.62	6.5
PC ₅₀ /PS ₅₀ + 20 wt% GO/ZrO ₂	332.45	348.38	392.10	411.55	7.8
PC ₅₀ /PS ₅₀ + 5 wt% DES-GO/ZrO ₂	334.52	352.62	394.52	414.52	9.3
PC ₅₀ /PS ₅₀ + 20 wt% DES-GO/ZrO ₂	336.69	354.62	396.65	418.52	11.6
PC ₅₀ /PS ₅₀ + 5 wt% ZrO ₂	342.52	361.52	399.62	420.26	13.5
PC ₅₀ /PS ₅₀ + 20 wt% ZrO ₂	345.65	363.98	400.12	423.52	18.6

6.3.5 Contact Angle Analysis

The contact angle has been identified in the droplet form at the liquid-vapor interface, which is located where the solid-liquid and liquid-vapor interfaces meet. A surface cannot be wet if the contact angle is more than 90°; instead, a bead of liquid will remain on the surface. The lotus effect is shown by an extremely hydrophobic surface with a contact angle of 110°, in which the droplet rapidly rolls down without contacting the surface. However, wetting the surface is desirable when the contact angle is less than 90°, as shown by the liquid's propensity to spread over a significant section of the surface while in contact [73–75]. The surface hydrophilicity to hydrophobic composite GO, ZrO₂, GO/ZrO₂, and DES-GO/ZrO₂ membranes at 50 mg/m² loading was assessed using contact angle measurements. **Figure 6.6** shows that the PC₅₀/PS₅₀+ 20 wt% GO produced the lowest contact angle (80.56°), indicating its hydrophilic nature due to the high concentration of hydrophilic oxygen functional groups. This is comparable with studies of

the contact angle ranges for GO, ZrO₂, GO/ZrO₂, and DES-GO/ZrO₂ hydrophilic membranes. The contact angle for GO/ZrO₂ membranes increases to 93.78°, while it increases to 98.12° & 104.23° for DES-GO/ZrO₂ & ZrO₂ membranes, as a result of oxygen functional group decrease. Furthermore, the hydrophilicity of the GO/ZrO₂ membrane is lower than that of the DES-GO/ZrO₂ & ZrO₂ membrane due to the steady decline with increasing DES functionalization time. For all ZrO₂ and DES-GO/ZrO₂ membranes, however, they have contact angle values inside the hydrophobic area (i.e., contact angle above 90°), which may be responsible for their increased gas permeability [72].

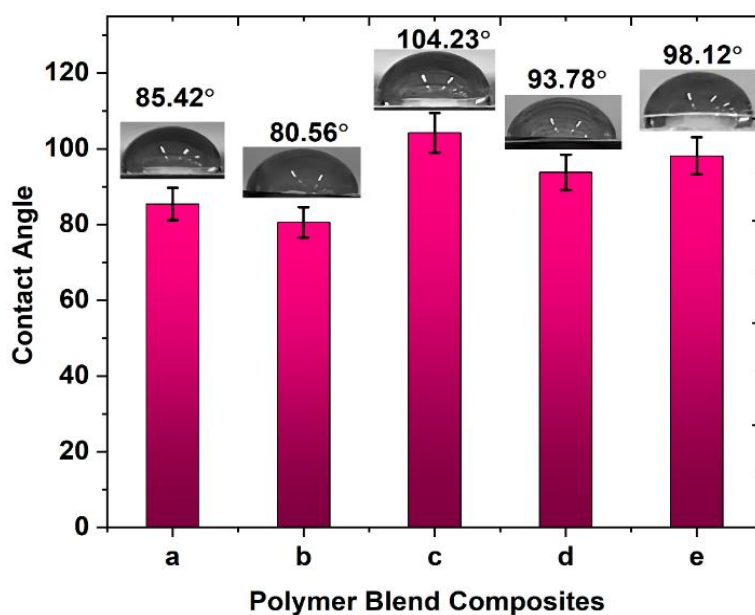


Figure 6.6: Contact angle measurements of (a) PC₅₀/PS₅₀ (b) PC₅₀/PS₅₀+ 20 wt% GO (c) PC₅₀/PS₅₀+ 20 wt% ZrO₂ (d) PC₅₀/PS₅₀+ 20 wt% GO/ZrO₂ (e) PC₅₀/PS₅₀+ 20 wt% DES-GO/ZrO₂.

6.3.6 Thickness and Porosity Measurements

It was observed that increasing membrane porosity increases microcapsule strength and membrane permeability because it provides stability to the mass transfer of chemicals across the membrane surface. In all membrane separation procedures, the porosity of the membrane plays a significant role in determining how well it performs [76]. There are various ways to determine porosity, such as mercury intrusion and gas adsorption, but the dry-wet weight method is most suitable for determining the effective porosity of microporous membranes [77]. The thickness and porosity of the membranes for the PC₅₀/PS₅₀ blend and blend composites with different nanofillers GO, ZrO₂, GO/ZrO₂ and DES-GO/ZrO₂ membranes are shown in **Figure 6.7 (i) and (ii)**. The porosity of PC₅₀/PS₅₀+ GO, PC₅₀/PS₅₀+ ZrO₂, PC₅₀/PS₅₀+ GO/ZrO₂ increased from 45% to 76%, 45% to 82%, 45% to 85%, respectively (**Figure 6.7 (ii)**). The porosity of

PC₅₀/PS₅₀+ DES-GO/ZrO₂ (2 wt% to 20 wt%) is very high, as we increased the wt% of DES-GO/ZrO₂ fillers in a blend of PC₅₀/PS₅₀ than porosity was increased significantly (from 45 % to 89 %) and that type of results we are expecting this blending is very useful for such kind of hydrogen gas applications. In **Figure 6.7 (i)**, the thickness of the membranes did not result in a significant increase or decrease as we changed the increased wt% of GO, ZrO₂, GO/ZrO₂, and DES-GO/ZrO₂ nanofillers, which means that membrane thickness may not be a critical factor in determining membrane permeability measurements [78].

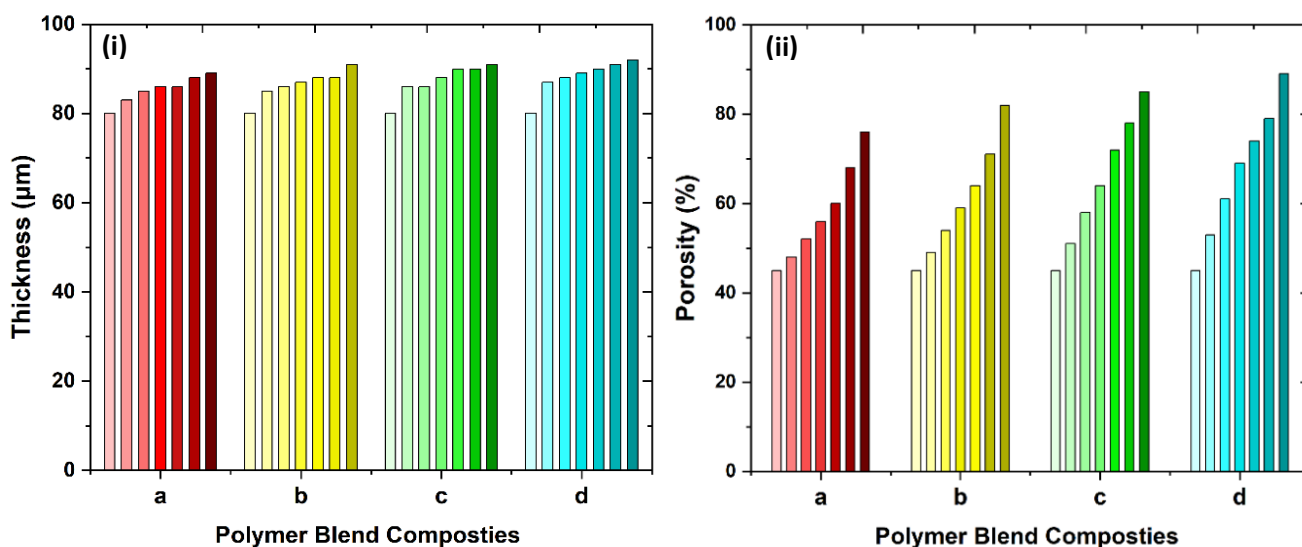


Figure 6.7: (i) Thickness (µm) and (ii) porosity (%) of (a) Blend of PC₅₀/PS₅₀ & PC₅₀/PS₅₀+ different wt% of GO (2 wt% to 20 wt%) (b) Blend of PC₅₀/PS₅₀ & PC₅₀/PS₅₀+ different wt% of ZrO₂ (2 wt% to 20 wt%) (c) Blend of PC₅₀/PS₅₀ & PC₅₀/PS₅₀+ different wt% of GO/ZrO₂ (2 wt% to 20 wt%) (d) Blend of PC₅₀/PS₅₀ & PC₅₀/PS₅₀+ different wt% of DES/GO/ ZrO₂ (2 wt% to 20 wt%), respectively.

These findings align with previous research, which observed that the addition of more nanofillers to a material led to increased porosity and void size, as illustrated in **Figure 6.7 (ii)**. As porosity increases, permeability also increases. Porosity measures a material's void spaces, while permeability measures a material's ability to transfer gas molecules or fluids. Porosity and permeability are properties common to all materials and permeability is a measure of how easily a fluid flows through a porous material and material may be extraordinarily porous, yet it has no permeability if the pores are not interconnected. Similarly, a material may have a few continuous pores that permit fluid movement, yet when porosity is calculated, the material does not seem to be extremely porous. Although not all voids are open at both ends, the effective porosity of the membrane is defined as the ratio of the related pore volume to the overall void volume. The

stiffness of the porous network is regulated by the solid phase, which forms the pore walls. As the number of holes along the width was increased by increasing the wt% of DES-GO/ZrO₂, the porous structure with smaller pores exhibited a better capacity to tolerate flow stress. In other words, samples with bigger pore sizes deformed more than those with smaller pore sizes, suggesting more flexible behaviour.

6.3.7 Mechanical Properties

The addition of GO/ZrO₂ nanoparticles to the PC₅₀/PS₅₀ matrix can enhance the material's tensile strength, Elongation modulus, Flexural strength, and Impact strength, which improved by 32.1%, 97.6%, 16.2% and 71.8% at maximum, respectively, when the DES-GO/ZrO₂ addition was 20 wt% in a blend of PC/PS, which is shown in **Figure 6.8 (i) to (iv)**. Additionally, the DES-GO/ZrO₂ showed greater tensile strength and flexural strength than the blend PC₅₀/PS₅₀, blend composite of PC₅₀/PS₅₀ + GO, PC₅₀/PS₅₀ + ZrO₂, PC₅₀/PS₅₀ + GO/ZrO₂. The interaction between hybrid particles of GO, ZrO₂, and the PC₅₀/PS₅₀ blends at both physical and chemical levels significantly increased the mechanical toughness of nanocomposite blend membranes [78]. In comparison to only blends of PC₅₀/PS₅₀ polymer, the tensile strength for PC₅₀/PS₅₀ + DES-GO/ZrO₂ nanocomposites is very good, and as we increased DES-GO/ZrO₂ wt% the tensile strength became stronger (**Figure 6.8 (i)**). The cross-section progressively increased as we increased DES-GO/ZrO₂ wt% showing many interactions between DES-GO/ZrO₂ and PC, PS. The DES-GO/ZrO₂ acts as a crosslinking site to connect with the polymeric chain in the composite membrane, increasing stiffness. However, when the amount of hybrid particles in the composites increased from 2 wt% to 20 wt%, their strength started to increase [75,79]. Agglomerated fillers inhibited the interface contact between the GO and ZrO₂ and the matrix because the dispersion of hybrid particles in the PC₅₀/PS₅₀ blends decreased with the increase in filler amount. When blend composites films were compared to only blended films, improvements in mechanical strength were seen. The highest tensile strength is 168 MPa, the highest flexural strength is 104 MPa and the highest impact strength is 210 J/m. Significant improvements in strain and toughness were observed in the case of DES-GO/ZrO₂. In this respect, when we composite with DES-GO/ZrO₂, we get the highest tensile strength as compared to the composite with GO, ZrO₂, and GO/ZrO₂. When compared to GO, ZrO₂, and GO/ZrO₂, DES-GO/ZrO₂ composites have a higher Young's modulus. This may be attributed to the strong molecule interaction between DES, GO, and ZrO₂. Notably, the DES-GO/ZrO₂ composite's Flexural strength was dramatically increased from 83 MPa to 103 MPa (**Figure 6.8 (iii)**). The resulting membrane film PC₅₀/PS₅₀ + DES-GO/ZrO₂ showed elastic performance with a fracture elongation and Young's modulus respectively, after increasing the DES-GO/ZrO₂ content from

2 wt% to 20 wt%. These results showed that the PC₅₀/PS₅₀ + DES-GO/ZrO₂ composite film produced by linking the stiff with PC₅₀/PS₅₀ nano-network template and the composite DES-GO/ZrO₂ provided both better elastic behaviour and significant tensile strength. This DES-GO/ZrO₂ composite, which may form more interfacial bonds with the polymer chain-end groups of PC₅₀/PS₅₀, may be the cause of the improved tensile strength from 115 Mpa to 168 Mpa. Chain mobility has increased due to this crosslinking, and the tensile strength started to increase at 118 MPa, resulting from the enhanced crosslinking of the DES-GO/ZrO₂ composite with PC₅₀/PS₅₀ blends. This increased crosslinking has provided additional strength to PC₅₀/PS₅₀ + DES-GO/ZrO₂ blend composite membranes [59].

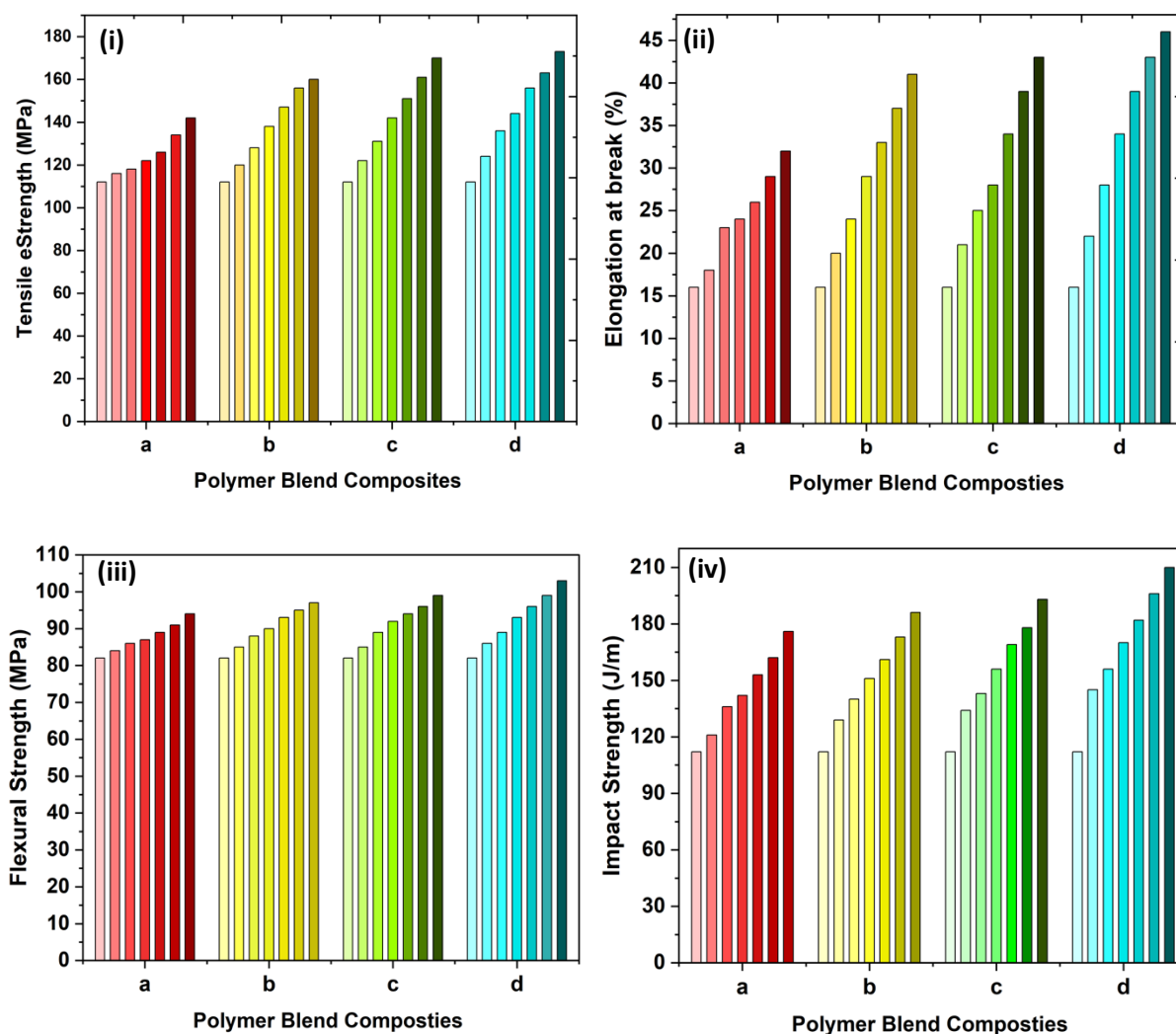


Figure 6.8: (i) Tensile strength (MPa) (ii) Elongation at break (%) (iii) Flexural strength (MPa) and (iv) Impact strength (J/m) of (a) Blend of PC₅₀/PS₅₀ & PC₅₀/PS₅₀+ different wt% of GO (2 wt% to 20 wt%) (b) Blend of PC₅₀/PS₅₀ & PC₅₀/PS₅₀+ different wt% of ZrO₂ (2 wt% to 20 wt%) (c) Blend of PC₅₀/PS₅₀ & PC₅₀/PS₅₀+ different wt% of GO/ZrO₂ (2 wt% to 20 wt%) (d) Blend of PC₅₀/PS₅₀ & PC₅₀/PS₅₀+ different wt% of DES-GO/ZrO₂ (2 wt% to 20 wt%).

Figure 6.9 shows Young's modulus of the PNCs membrane films. The films of DES-GO/ZrO₂ composites exhibit higher Young's modulus values compared to the films of other composite membranes such as GO, ZrO₂, and GO/ZrO₂, which have lower Young's modulus [22,26]. Young's modulus of DES-GO/ZrO₂ at ideal preparation circumstances was 3836 N/mm² more than that of the GO/ZrO₂ composite film. The results of the studies carried out on GO/ZrO₂ composites films synthesized in DES solvent provided the greatest improvement of the mechanical characteristics. Because the ZrO₂ was far more rigid than GO, all PNCs had an increasing interest in Young's modulus. As a result, all NCs were stiffer after including ZrO₂ and the improved thermal stability of PC₅₀/PS₅₀ brought on by the inclusion of GO was also a strong supporter of the increase in Young's modulus.

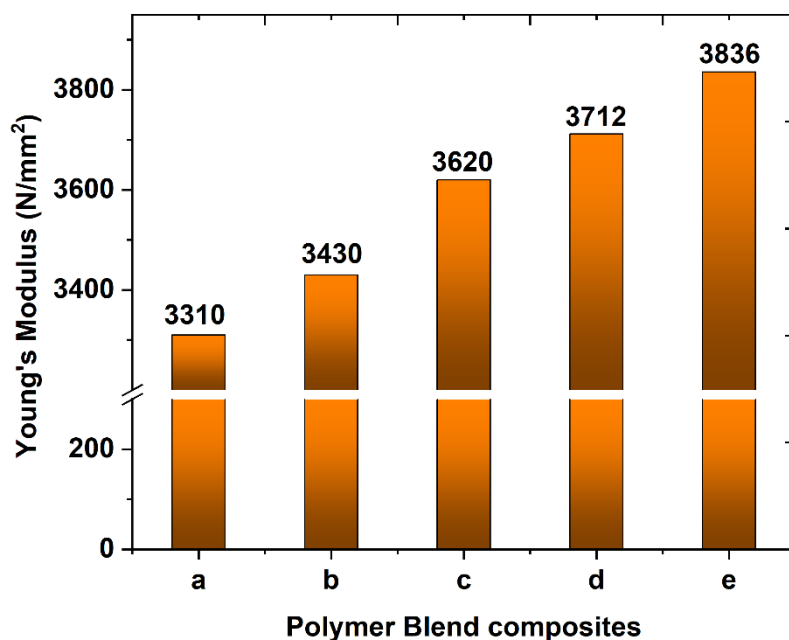


Figure 6.9: Young's modulus (N/mm²) of (a) blend of PC₅₀/PS₅₀ (b) PC₅₀/PS₅₀+ 20 wt% GO (c) PC₅₀/PS₅₀+ 20 wt% ZrO₂ (d) PC₅₀/PS₅₀+ 20 wt% GO/ZrO₂ (e) PC₅₀/PS₅₀+ 20 wt% DES/GO/ZrO₂.

6.3.8 Gas permeability

In this present study, glassy membrane compositions such as PC and PS are used as base materials, and the transport of gas molecules through the dense medium follows the solution-diffusion mechanism [80]. According to this model, the feed gas is first adsorbed from the upstream side of the membrane surface, diffuses across the membrane thickness, and lastly, desorption takes place from the downstream side of the membrane. To obtain higher permeability without compromising the separation factor, a new generation of hybrid materials significantly enhances the adsorption-desorption as well as diffusion mechanism, which affects the overall gas

transport parameters. The present hybridization includes a blend of two different glassy phases along with DES based filler composition. **Figure 6.10 (i) to (iv)** depicts the gas permeability of various MMMs. The gain in permeability follows the sequence such as $H_2 > CO_2 > N_2 > O_2 > CH_4$ according to the kinetic diameter of gases. H_2 being the smallest kinetic diameter diffuses faster compared to the rest of the gases. Hence, it gives higher permeability.

Figure 6.10 (i) represents the permeability of various feed gases across GO embedded PC/PS blend membranes. The introduction of GO into the glassy phase significantly enhances permeability in a positive manner. As the filler content is increased up to 20 wt%, the permeability of all the applied feed gases increases. The H_2 permeability coefficient improves by more than twofold as the GO amount is increased from 0 wt% to 20 wt%. CO_2 permeability almost doubles, and it also enhances the permeability of the other gases. This promising result is attributed to the characteristics of GO sheets, which create a large number of tortuous paths to enhance gas diffusion. This diffusion path depends on the kinetic diameter of the gas molecule. Moreover, there is a strong interface interaction between GO and the polymer phase which limits polymer chain mobility. As a consequence, the activation energy of permeating gases is improved [81]. Furthermore, the introduction of GO flakes into the polymer matrix forms interfacial voids between GO and polymer chains which in turn results in fractional free volume. As the filler amount is further increased, Fraction free volume (FFV) also escalates and finally catalyses mass transport parameters [82]. It can be observed that CO_2 also diffuses at a similar speed to H_2 , despite its larger kinetic diameter compared to H_2 . This result, particularly for CO_2 is due to its adsorption-diffusion property. As per the XRD analysis, the reduced crystallinity facilitates faster diffusion and increase CO_2 sorption as a consequence of the amino group present in the polymer backbone. In addition, the GO-flakes increases active CO_2 sorption along its surface which in turn improves CO_2 solubility in the polymer matrix. CO_2 is a non-polar gas but due to the polarity of individual C-O bonds confirms the molecular interaction with carboxylic groups in GO. Thus, carboxylic acid groups in GO provide a preferential sorption site to CO_2 gas molecules. In addition, the structural defect on the GO surface also acts as nanopores and strongly traps gas species [83,84].

From **Figure 6.10 (ii)**, as the ZrO_2 content is increased from 0 wt% to 20 wt%, the permeability of all the gas molecules is enhanced. H_2 permeability increases by more than three-fold, while for the other gases, it improves by more than two-fold. In this case, the filler concentration influences the formation of surface pores in the resulting membrane. During the membrane casting process, the introduction of ZrO_2 fillers creates surface pores due to stress. Thus, the surface porosity of ZrO_2 influences membrane skin porosity and overall gas

permeability. While both nano-fillers have individually influenced gas permeability to some extent, their combined effect significantly enhances the results, as depicted in **Figure 6.10 (iii)**. The highest permeability is achieved with H₂ gas for a 20 wt% GO/ZrO₂ composition, which is around 63 Barrer, more than six times higher than that of the pure blend membrane. CO₂ permeability increases by 22 Barrer for the highest filler content, more than three times the base value. The other gases also showed a drastic improvement of almost four times enhancement in the final permeability coefficient. This outcome may be due to the combined effect of both penetrants which improved fractional free volume along with surface porosity.

Notably, a more significant change is observed in **Figure 6.10 (iv)**, where the permeability of gases increases when DES-GO/ZrO₂ implanted MMMs are used in the gas permeation test. Superior performance is evident, particularly for the faster-permeating H₂ gas molecule, resulting in a peak gas permeability coefficient of around 86 Barrers, which is more than eight times higher than that of the original blend membrane. The next notable improvement is observed in N₂ gas permeability, increasing from 4.8 Barrer to 24.63 Barrer. This represents a drastic change, approximately five times higher than the base value. Again, this is a drastic change which is around three times than the base value. Gas permeability for the rest of the gases also improves more than four times showing superior performance of the hybridized membranes. As referenced by Hansen, et al. [85], DES provides intermolecular attraction to the guest penetrating species. Thus, the adsorption capacity of the composite membrane improves. DES has a specific Van der Waals interaction with CO₂ gas resulting in its higher solubility. As the sorption coefficient is also a responsible gas transport parameter provides higher CO₂ permeability [86]. The involvement of DES in the polymer matrix improves the thermodynamic stability of the resultant membrane. It also gains the viscosity of membrane solution resulting in the decrease of phase separation. This effect can form large uniform pores on the skin layer and develop micro-voids in the support layer. Thus, DES modified GO/ZrO₂ forms uniform pores on the membrane surface and micro-voids within the membrane matrix. This outcome can improve membrane performance in terms of diffusion of gas molecules and their permeability [57]. Moreover, from the contact angle analysis, the introduction of ZrO₂ and DES functionalization increases the hydrophobicity of the final product by reducing oxygen functional group which in turn fosters gas permeability. In addition, the filler content has stimulated the membrane porosity conformed by the porosity determination experiment. As the weight percentage of GO, ZrO₂, GO-ZrO₂, and DES-GO/ZrO₂ is increased, the void size as well as porosity increases additional transport routes to the applied feed gas. Even from the XRD analysis, it can be observed that DES-supported membranes improve the interlayer spacing, enhancing the diffusion of gas molecules. The agglomeration due to fillers causes free

spaces at the nanoparticle and polymer interaction surface which is clearly indicated in SEM analysis. According to the characterization, large sized agglomerated particles exist within the membrane surface. This free space provides a smaller diffusion path to the penetrant and assists the penetrant in transport.

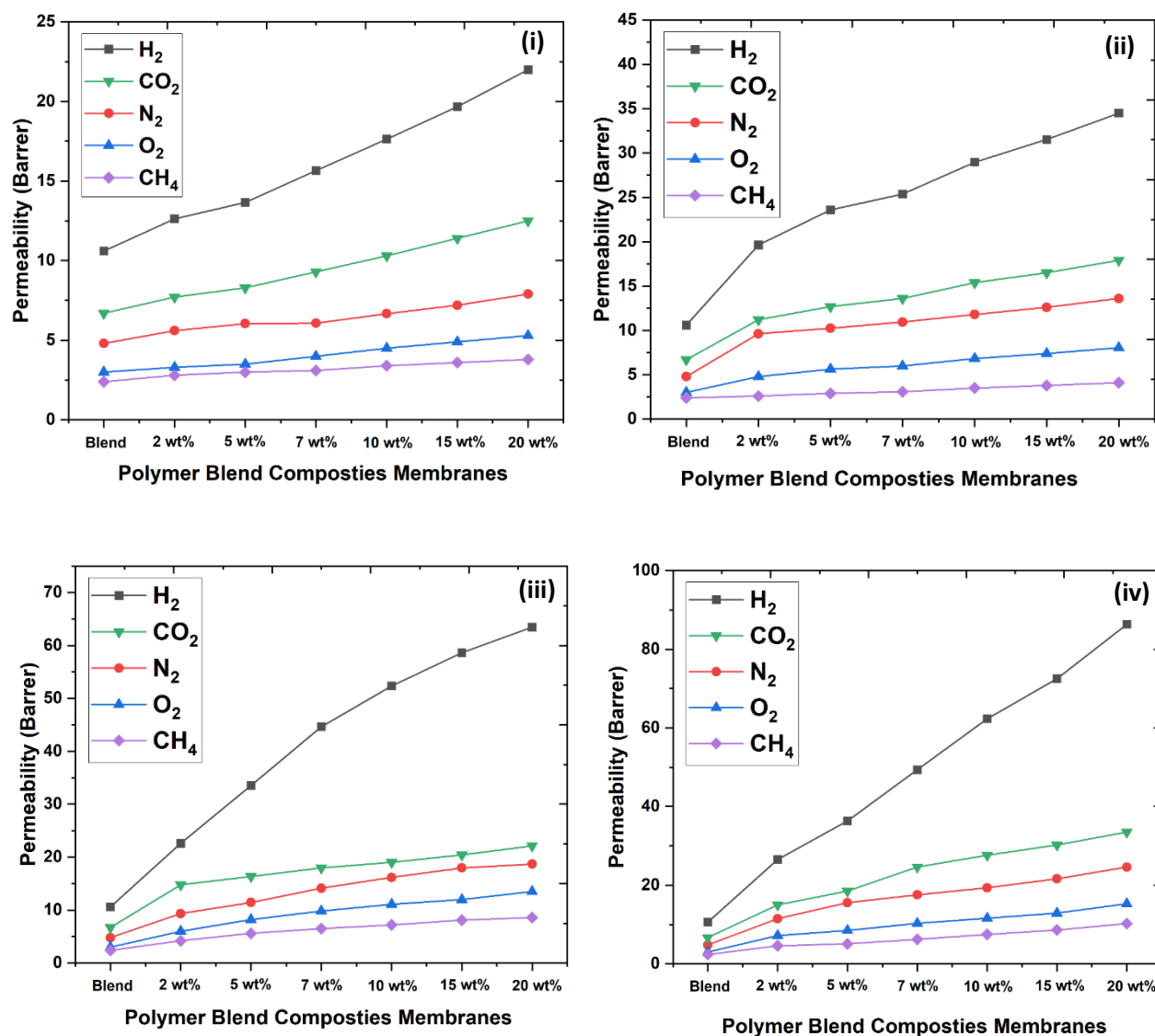


Figure 6.10: Gas permeability of H₂, CO₂, N₂, O₂ and CH₄ in (i) GO (ii) ZrO₂ (iii) GO/ZrO₂ (iv) DES-GO/ZrO₂ with 0 wt% to 20 wt% nanofillers.

6.3.9 Selectivity and upper bound visualization

The separation of gases usually relies on the nature of the host membrane composition. When discussing the selectivity of particular gas pairs, it becomes essential to introduce Robeson's trade-off relationship between selectivity and permeability for the hybrid membranes [24,25]. Generally, when one of these parameters' uplifts, the other is sacrificed. However, certain

membrane compositions have significantly improved both the gas permeability coefficient and the separation factor. **Figure 6.11 (i-iv)** shows the selectivity of gases with respect to the various membrane compositions, while **Figure 6.12 (i-iv)** sheds light on hydrogen separation from other gas mixtures. When focusing on H₂ separation from the other gases, H₂ having a kinetic diameter of 2.89 Å transports faster as compared to other gases from the GO-derived nano-channels. The other gases such as N₂, O₂, and CH₄ cannot transport through the nano-channels as the nano-channels exist around 3.5 Å interlayer height. Furthermore, the FFV also provides diffusion pathways to the smaller kinetic diameter gases such as H₂ and CO₂. As a result, the selectivity for H₂/N₂, H₂/O₂ and H₂/CH₄ is higher than that for H₂/CO₂ selectivity. H₂/CH₄ shows a higher value than other gas pairs because H₂ molecules can swiftly pass through the free volume of the membrane to the permeate side, while CH₄ molecules accumulate in the interlayer gallery of GO. Moreover, CH₄ shows a strong affinity with GO as compared to H₂. These factors promote H₂ separation from CH₄ [87]. For the single gas permeation experiment, the separation of H₂ from CO₂ is a molecular sieving operation since CO₂ species are strongly absorbed by the GO flakes. However, CO₂ does not fit into every structural defect created by GO and ZrO₂, it permeates through a few quantities of large defects [88].

In the case of the H₂/CO₂ gas pair (**Figure 6.12 (i)**), the interaction of GO within the blend composition alters the selectivity with a smaller magnitude whereas ZrO₂/PC-PS provides a better outcome. However, when GO along with ZrO₂ results in better separation of H₂ from CO₂. Notably, as the filler content is magnified up to 20 wt%, the selectivity becomes more than double, which tends the material towards Robeson's boundary limit. Additionally, DES modified fillers enhance H₂/CO₂ selectivity along with permeability. The trade-off relationship for H₂/CO₂ is given in **Figure 6.12 (i)**. The plot clearly shows that as the filler content is increased, the membrane composition tends towards the trade-off line. Moreover, at the highest particle loading, the fabricated MMM crosses the Robeson's 2008 upper bound [24], which makes the material in a novel group of hybridized membranes. Then after the H₂/N₂ selectivity gains with almost the same value for both individual filler compositions. However, the integration of GO/ZrO₂ and DES-GO/ZrO₂ provides promising output, as depicted in **Figure 6.12 (iv)**, with the modified composition leading towards the Robeson's 1991 upper bound [25]. A similar trend in membrane composition is observed for H₂/O₂ selectivity, as shown in **Figure 6.12 (iii)**. Due to a large difference between the kinetic diameter of H₂ and CH₄, their separation factor tremendously boosts when GO/ZrO₂ and DES-GO/ZrO₂ are embedded into the blend phase. **Figure 6.12 (ii)** presents the trade-off plot for H₂/CH₄, with the 20 wt% DES-GO/ZrO₂ lying below the 1991

boundary line. This outstanding performance of hydrogen separation can be applicable in multifarious energy applications [2,37,89].

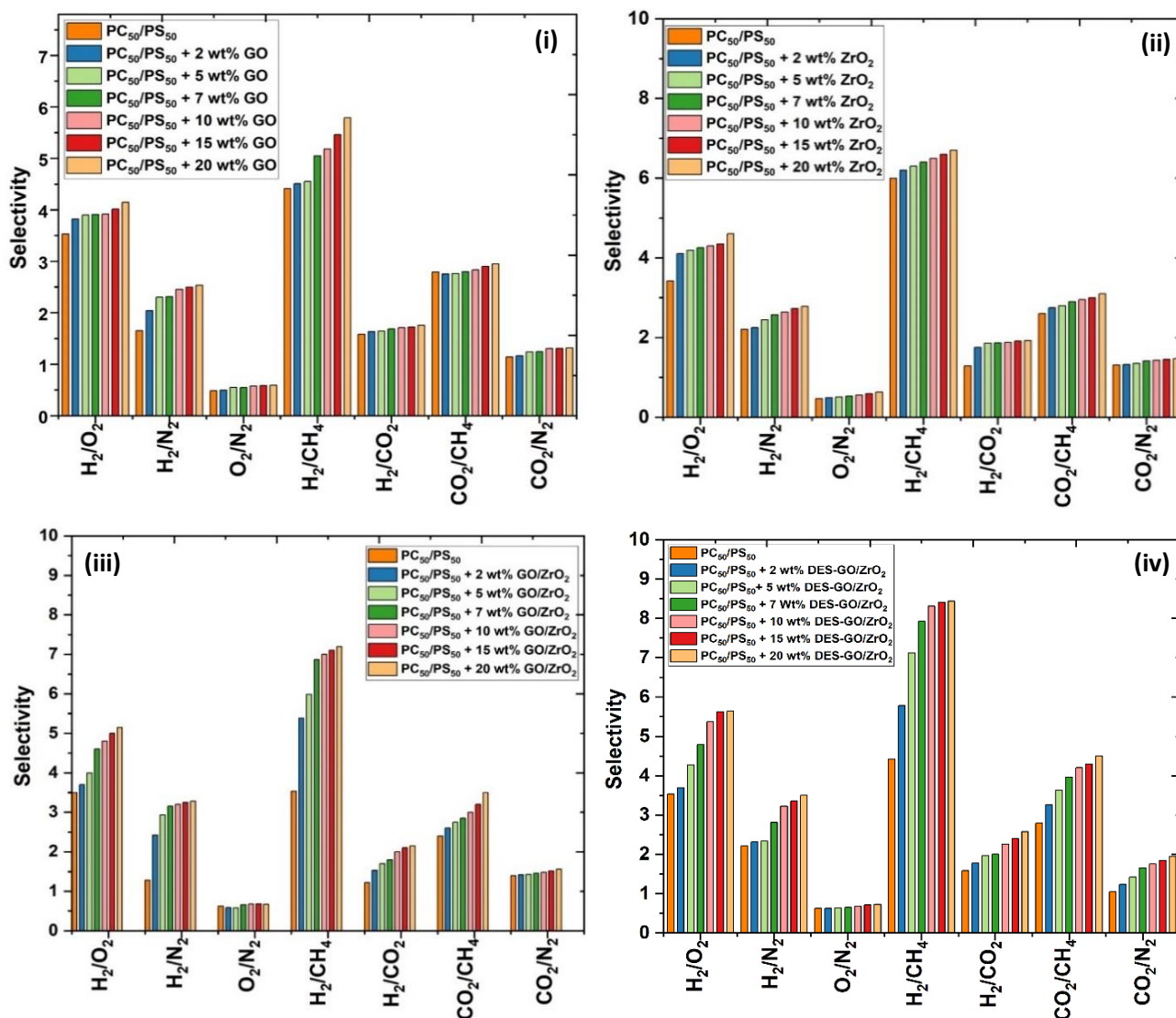


Figure 6.11: Gas selectivity of PC₅₀/PS₅₀ + 2 wt% to 20 wt% nanofillers (i) GO (ii) ZrO₂ (iii) GO/ZrO₂ (iv) DES-GO/ZrO₂ in various gases.

The MMMs also demonstrate favourable results in the separation of CO₂ from N₂ and CH₄. While CO₂/N₂ selectivity improves linearly with the addition of any of the additives, the polymer membrane implanted with DES-GO/ZrO₂ shows particularly noteworthy results. Such a modification is applicable in natural gas purification, CO₂ capturing, and compositional flue gas treatment, where CO₂ is separated from the CH₂ and N₂ gases [90]. Specifically, CO₂ molecules diffuse faster than N₂ and CH₄ due to their adsorption and diffusion properties with GO. Moreover, the functional groups on DES enhance the selectivity and permeability of CO₂ in MMM, due to its greater affinity or attraction for CO₂ [91]. What is more, as the DES concentration increases, the diffusion of CO₂ enhances, altering the morphology of MMMs and

allowing accessible vacancies for the passage of CO₂ molecules [92]. Even the interdiction of GO sheets modifies the CO₂/N₂ selectivity due to surface-functional groups, a high aspect ratio, varying orientations of the nanofillers, and high compatibility with the glassy phase [81]. Furthermore, the interaction between the –COOH and –OH polar groups on GO nanosheets and the CO₂ host membrane exhibit stronger CO₂ adsorption ability compared to pure polymeric material. Even MMMs composed of GO provide preferential CO₂ adsorption and transport, which is essential for generating fast and selective nanochannels for CO₂ gas molecules [93].

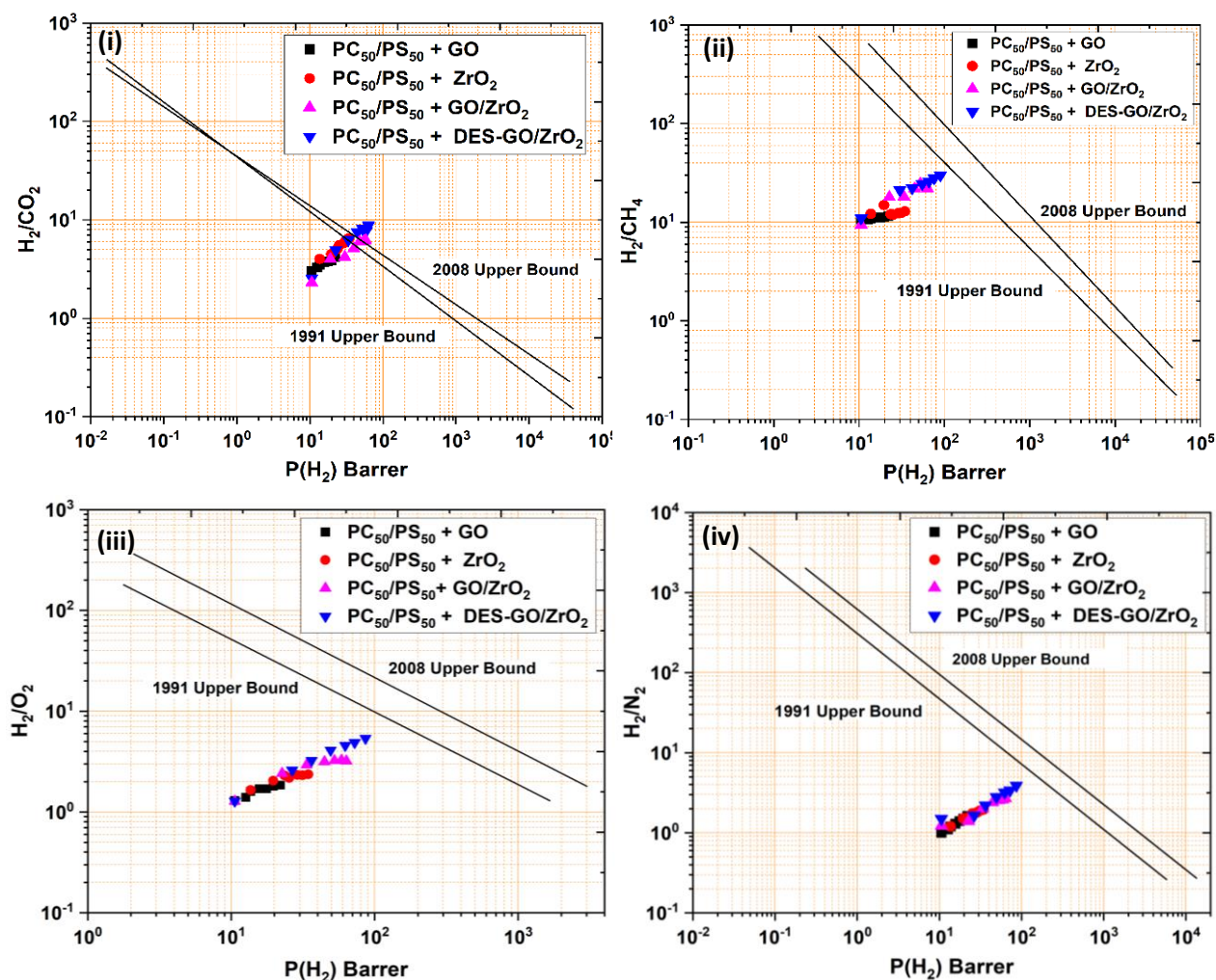


Figure 6.12: Robeson upper bound correlations for (i) H₂/CO₂ separation (ii) H₂/CH₄ separation (iii) H₂/O₂ separation and (iv) H₂/N₂ separation in PC₅₀/PS₅₀ + 20 wt% nanofillers (GO, ZrO₂, GO/ZrO₂ and DES-GO/ZrO₂).

Last but not least, O₂/N₂ separation also serves a similar trend to the other gas pairs. Moreover, again DES modified membrane shows an immense separation performance. Such an outcome can be applicable to oxygen enrichment, gasification, natural gas purification as well as the oxyfuel combustion process where it becomes a prerequisite to separate O₂ from the N₂ or

other air products [94,95]. Thus, a significant trade-off between gas selectivity and permeability has been achieved by the combination of glassy polymers, GO/ZrO₂ nanofillers, and DES, which evaluates the membrane's performance.

6.4 Conclusion

Permeability/selectivity data for various environmental gases were computed on the basis of the variation in the rate of permeation with time. Modification of PNCs with various fabricated nanofillers shows a distinct (8-fold increase is observed over the starting polymer blend) improvement in permeability, with the highest value with DES modified nanofiller. This is proposed due to the synergy developed (e.g., surface porosity) among the components of DES based MMM. Additionally, this modified nanofiller based MMM shows a distinct raise in thermal and mechanical strength (increases by 97.6 % for 20 wt% of DES-GO/ZrO₂), which is a prerequisite for the application of MMMs for pure hydrogen production. A prominent upshot of this synergism was achieved using state-of-the-art Robeson's upper bound visualization. The MMMs tend toward the trade-off boundary and the outstanding remark can be noticed for H₂/CO₂ selectivity (crosses the boundary line). Such performance can attract vast industrial applications, especially for energy applications and hydrogen purification. Exploring the above class of modified MMMs and their utilization in medical applications, hydrocarbon reforming as well as separation and syngas production could be a future line of research.

6.5 References

- [1] N. A. Shepelin, A. M. Glushenkov, V. C. Lussini, P. J. Fox, G. W. Dicoski, J. G. Shapter, and A. V. Ellis, *Energy Environ Sci* **12**, 1143 (2019).
- [2] Q. Hassan, A. Z. Sameen, H. M. Salman, M. Jaszczur, and A. K. Al-Jiboory, *J Energy Storage* **72**, 108404 (2023).
- [3] S. Krevor, H. de Coninck, S. E. Gasda, N. S. Ghaleigh, V. de Gooyert, H. Hajibeygi, R. Juanes, J. Neufeld, J. J. Roberts, and F. Swennenhuis, *Nat Rev Earth Environ* **4**, 102 (2023).
- [4] M. A. Khan, T. Al-Attas, S. Roy, M. M. Rahman, N. Ghaffour, V. Thangadurai, S. Larter, J. Hu, P. M. Ajayan, and M. G. Kibria, *Energy Environ Sci* **14**, 4831 (2021).
- [5] M. Amin, H. H. Shah, A. G. Fareed, W. U. Khan, E. Chung, A. Zia, Z. U. Rahman Farooqi, and C. Lee, *Int J Hydrogen Energy* **47**, 33112 (2022).
- [6] P. J. Megía, A. J. Vizcaíno, J. A. Calles, and A. Carrero, *Energy & Fuels* **35**, 16403 (2021).
- [7] T. Yusaf, A. S. Faisal Mahamude, K. Kadirgama, D. Ramasamy, K. Farhana, H. A. Dhahad, and A. R. Abu Talib, *Int J Hydrogen Energy* (2023).
- [8] I. Moradpoor, S. Syri, and A. Santasalo-Aarnio, *Renewable and Sustainable Energy Reviews* **175**, 113159 (2023).
- [9] M. Hirscher, V. A. Yartys, M. Baricco, J. Bellosta von Colbe, D. Blanchard, R. C. Bowman, D. P. Broom, C. E. Buckley, F. Chang, P. Chen, Y. W. Cho, J.-C. Crivello, F. Cuevas, W. I. F. David, P. E. de Jongh, R. V. Denys, M. Dornheim, M. Felderhoff, Y. Filinchuk, G. E. Froudakis, D. M. Grant, E. MacA. Gray, B. C. Hauback, T. He, T. D. Humphries, T. R. Jensen, S. Kim, Y. Kojima, M. Latroche, H.-W. Li, M. V. Lototskyy, J. W. Makepeace, K. T. Møller, L. Naheed, P. Ngene, D. Noréus, M. M. Nygård, S. Orimo, M. Paskevicius, L. Pasquini, D. B. Ravnsbæk, M. Veronica Sofianos, T. J. Udovic, T. Vegge, G. S. Walker, C. J. Webb, C. Weidenthaler, and C. Zlotea, *J Alloys Compd* **827**, 153548 (2020).
- [10] L. Fan, Z. Tu, and S. H. Chan, *Energy Reports* **7**, 8421 (2021).
- [11] M. C. Vásquez, E. E. Silva, and E. F. Castillo, *Biomass Bioenergy* **105**, 197 (2017).
- [12] S. A. Brough, S. H. Riley, G. S. McGrady, S. Tanhawiriyakul, L. Romero-Zerón, and C. D. Willson, *Chemical Communications* **46**, 4923 (2010).

- [13] W. C. Nadaleti, E. G. de Souza, and S. N. M. de Souza, *Int J Hydrogen Energy* **47**, 34727 (2022).
- [14] A. M. Al-Bassam, J. A. Conner, and V. I. Manousiouthakis, *ACS Sustain Chem Eng* **6**, 3029 (2018).
- [15] J. George, P. Arun, and C. Muraleedharan, *Procedia Technology* **25**, 982 (2016).
- [16] P. Li, H. Z. Chen, and T.-S. Chung, *J Memb Sci* **434**, 18 (2013).
- [17] A. K. Patel and N. K. Acharya, *Int J Hydrogen Energy* **45**, 18685 (2020).
- [18] C. Z. Liang, T.-S. Chung, and J.-Y. Lai, *Prog Polym Sci* **97**, 101141 (2019).
- [19] N. Pal, M. Agarwal, K. Maheshwari, and Y. S. Solanki, *Mater Today Proc* **28**, 1386 (2020).
- [20] M. Weber, M. Drobek, B. Rebière, C. Charmette, J. Cartier, A. Julbe, and M. Bechelany, *J Memb Sci* **596**, 117701 (2020).
- [21] H. G. Shiraz and M. G. Shiraz, *Int J Hydrogen Energy* **42**, 11528 (2017).
- [22] A. Patel and N. K. Acharya, *Nanomaterials and Energy* **10**, 101 (2021).
- [23] P. S. Goh, A. F. Ismail, S. M. Sanip, B. C. Ng, and M. Aziz, *Sep Purif Technol* **81**, 243 (2011).
- [24] L. M. Robeson, *J Memb Sci* **320**, 390 (2008).
- [25] L. M. Robeson, *J Memb Sci* **62**, 165 (1991).
- [26] A. K. Patel and N. K. Acharya, in *Trends and Applications in Advanced Polymeric Materials* (Wiley, 2017), pp. 191–206.
- [27] D. Şen, H. Kalıpçılar, and L. Yılmaz, *Sep Sci Technol* **41**, 1813 (2006).
- [28] N. K. Acharya, P. K. Yadav, and Y. K. Vijay, *Study of Temperature Dependent Gas Permeability for Polycarbonate Membrane*, 2004.
- [29] Y. Utievskiy, C. Neumann, J. Sindlinger, K. Schutjajew, M. Oschatz, A. Turchanin, N. Ueberschaar, and F. H. Schacher, *Nanomaterials* **13**, 2498 (2023).
- [30] S. Ashtiani, M. Khoshnamvand, D. Bouša, J. Šturala, Z. Sofer, A. Shaliutina-Kolešová, D. Gardenö, and K. Friess, *Int J Hydrogen Energy* **46**, 5449 (2021).
- [31] A. K. Patel and N. K. Acharya, *Int J Hydrogen Energy* **43**, 21675 (2018).

- [32] H. Kweon, C.-W. Lin, M. M. Faruque Hasan, R. Kaner, and G. N. Sant, *ACS Appl Polym Mater* **1**, 3233 (2019).
- [33] G. Liu, W. Jin, and N. Xu, *Chem Soc Rev* **44**, 5016 (2015).
- [34] L. Jiang and Z. Fan, *Nanoscale* **6**, 1922 (2014).
- [35] A. S. Nimbalkar, S. K. Tiwari, S. Kyu Ha, and C. Kook Hong, *Mater Today Proc* **21**, 1749 (2020).
- [36] A. Balaji, S. Yang, J. Wang, and J. Zhang, *Biosensors (Basel)* **9**, 74 (2019).
- [37] M. Sohail Ahmad, Y. Inomata, and T. Kida, *The Chemical Record* (2023).
- [38] A. Halim, Q. Luo, Y. Ju, and G. Song, *Nanomaterials* **8**, 736 (2018).
- [39] A. Buekenhoudt, *Stability of Porous Ceramic Membranes* (2008), pp. 1–31.
- [40] A. Dashti and M. Asghari, *ChemBioEng Reviews* **2**, 54 (2015).
- [41] M. Padaki, R. Surya Murali, M. S. Abdullah, N. Misdan, A. Moslehyani, M. A. Kassim, N. Hilal, and A. F. Ismail, *Desalination* **357**, 197 (2015).
- [42] F. E. Bortot Coelho, G. Magnacca, V. Boffa, V. M. Candelario, M. Luiten-Olieman, and W. Zhang, *Ceram Int* **49**, 8683 (2023).
- [43] Y. Liu, L. Liu, Y. Yang, T. Yang, C. Li, S. Kawi, and X. Wang, *J Memb Sci* **684**, 121851 (2023).
- [44] S. Kitamura, T. Yoshioka, K. Nakagawa, T. Kitagawa, Y. Okamoto, A. Matsuoka, E. Kamio, and H. Matsuyama, *Sep Purif Technol* **315**, 123576 (2023).
- [45] D. Hirpara, B. Patel, V. Chavda, A. Desai, and S. Kumar, *J Mol Liq* **364**, 119991 (2022).
- [46] D. Hirpara, B. Patel, V. Chavda, and S. Kumar, *J Mol Liq* **362**, 119672 (2022).
- [47] V. Chavda, D. Hirpara, and S. Kumar, *J Mol Liq* **368**, 120614 (2022).
- [48] Y. Ji, Z. Meng, J. Zhao, H. Zhao, and L. Zhao, *J Chromatogr A* **1609**, 460520 (2020).
- [49] Y. Wang, K. H. Kim, K. Jeong, N.-K. Kim, and C. G. Yoo, *Curr Opin Green Sustain Chem* **27**, 100396 (2021).
- [50] Y. Chen and T. Mu, *Green Energy & Environment* **4**, 95 (2019).

- [51] Y. Liu, N. Deak, Z. Wang, H. Yu, L. Hameleers, E. Jurak, P. J. Deuss, and K. Barta, *Nat Commun* **12**, 5424 (2021).
- [52] X. Liang, Y. Fu, and J. Chang, *Sep Purif Technol* **210**, 409 (2019).
- [53] R. Craveiro, L. A. Neves, A. R. C. Duarte, and A. Paiva, *Sep Purif Technol* **254**, 117593 (2021).
- [54] M. K. AlOmar, M. A. Alsaadi, M. Hayyan, S. Akib, R. K. Ibrahim, and M. A. Hashim, *J Mol Liq* **222**, 883 (2016).
- [55] P. A. Shah, V. Chavda, D. Hirpara, V. S. Sharma, P. S. Shrivastav, and S. Kumar, *J Mol Liq* **390**, 123171 (2023).
- [56] H. Lin, K. Gong, W. Ying, D. Chen, J. Zhang, Y. Yan, and X. Peng, *Small* **15**, 1904145 (2019).
- [57] M. Taghizadeh, A. Taghizadeh, V. Vatanpour, M. R. Ganjali, and M. R. Saeb, *Sep Purif Technol* **258**, 118015 (2021).
- [58] C. Bărdacă Urducea, A. C. Nechifor, I. A. Dimulescu, O. Oprea, G. Nechifor, E. E. Totu, I. Isildak, P. C. Albu, and S. G. Bungău, *Nanomaterials* **10**, 2349 (2020).
- [59] H. D. Patel and N. K. Acharya, *Int J Hydrogen Energy* (2023).
- [60] N. Panapitiya, S. Wijenayake, D. Nguyen, C. Karunaweera, Y. Huang, K. Balkus, I. Musselman, and J. Ferraris, *Materials*.
- [61] Y. Wu, X. Zhang, Y. Guo, and X. Wang, *ChemistrySelect* **4**, 10868 (2019).
- [62] G. García, S. Aparicio, R. Ullah, and M. Atilhan, *Energy and Fuels* **29**, 2616 (2015).
- [63] S. Wang, S. Zhou, J. Huang, G. Zhao, and Y. Liu, *J Mater Sci* **54**, 8247 (2019).
- [64] A. K. Zulkhairun, Z. G. Fachrurrazi, M. Nur Izwanne, and A. F. Ismail, *Sep Purif Technol* **146**, 85 (2015).
- [65] R. S. Das, S. K. Warkhade, A. Kumar, and A. V. Wankhade, *Research on Chemical Intermediates* **45**, 1689 (2019).
- [66] M. K. Pal, B. Singh, and J. Gautam, in *Journal of Thermal Analysis and Calorimetry*, Vol. 107 (2012), pp. 85–96.

- [67] G. Stefame³, S. Popovid, and S. Musid, *Thermochimica Acta Influence of PH on the Hydrothermal Crystallization Kinetics and Crystal Structure of ZrO₂*, 1997.
- [68] F. E. Bortot Coelho, N. N. Kaiser, G. Magnacca, and V. M. Candelario, *J Eur Ceram Soc* **41**, 7792 (2021).
- [69] F. Farivar, P. Lay Yap, R. U. Karunagaran, and D. Losic, *C (Basel)* **7**, 41 (2021).
- [70] J. Park, H. Ha, H. W. Yoon, J. Noh, H. B. Park, D. R. Paul, C. J. Ellison, and B. D. Freeman, *Polymer (Guildf)* **212**, (2021).
- [71] T. K. Mishra, A. Kumar, V. Verma, K. N. Pandey, and V. Kumar, *Compos Sci Technol* **72**, 1627 (2012).
- [72] Z. Yuan, W. Tian, F. Li, Q. Fu, X. Wang, W. Qian, and W. An, *J Alloys Compd* **822**, 153658 (2020).
- [73] J. C. Bird, S. Mandre, and H. A. Stone, *Phys Rev Lett* **100**, 234501 (2008).
- [74] D. Zhang, S. Takase, and G. Nagayama, *J Colloid Interface Sci* **591**, 474 (2021).
- [75] H. D. Patel and N. K. Acharya, *Chem Eng Technol* **45**, 2223 (2022).
- [76] L. Rodríguez-Jardón, M. López-González, M. Iglesias, and E. M. Maya, *J Memb Sci* **619**, 118795 (2021).
- [77] M. Zeng, Z. Fang, and C. Xu, *J Appl Polym Sci* **91**, 2840 (2004).
- [78] R. M. C. Santana and S. Manrich, *J Appl Polym Sci* **88**, 2861 (2003).
- [79] H. D. Patel and N. K. Acharya, *Polym Eng Sci* **61**, 2782 (2021).
- [80] J. G. Wijmans and R. W. Baker, *J Memb Sci* **107**, 1 (1995).
- [81] M. Asghari, S. Saadatmandi, and M. Afsari, *ChemBioEng Reviews* **8**, 490 (2021).
- [82] B. M. Yoo, J. E. Shin, H. D. Lee, and H. B. Park, *Curr Opin Chem Eng* **16**, 39 (2017).
- [83] H. W. Kim, H. W. Yoon, S.-M. Yoon, B. M. Yoo, B. K. Ahn, Y. H. Cho, H. J. Shin, H. Yang, U. Paik, S. Kwon, J.-Y. Choi, and H. B. Park, *Science (1979)* **342**, 91 (2013).
- [84] R. K. Joshi, S. Alwarappan, M. Yoshimura, V. Sahajwalla, and Y. Nishina, *Appl Mater Today* **1**, 1 (2015).

- [85] B. B. Hansen, S. Spittle, B. Chen, D. Poe, Y. Zhang, J. M. Klein, A. Horton, L. Adhikari, T. Zelovich, B. W. Doherty, B. Gurkan, E. J. Maginn, A. Ragauskas, M. Dadmun, T. A. Zawodzinski, G. A. Baker, M. E. Tuckerman, R. F. Savinell, and J. R. Sangoro, *Chem Rev* **121**, 1232 (2021).
- [86] R. Cabezas, E. Zurob, B. Gomez, G. Merlet, A. Plaza, C. Araya-Lopez, J. Romero, F. Olea, E. Quijada-Maldonado, L. Pino-Soto, T. Gonzalez, and R. Castro-Muñoz, *Ind Eng Chem Res* **61**, 17397 (2022).
- [87] H. Zheng, L. Zhu, D. He, T. Guo, X. Li, X. Chang, and Q. Xue, *Int J Hydrogen Energy* **42**, 30653 (2017).
- [88] H. Li, Z. Song, X. Zhang, Y. Huang, S. Li, Y. Mao, H. J. Ploehn, Y. Bao, and M. Yu, *Science* (1979) **342**, 95 (2013).
- [89] N. Devi, R. Kumar, S. Singh, and R. K. Singh, *Critical Reviews in Solid State and Materials Sciences* **1** (2022).
- [90] M. Chawla, H. Saulat, M. Masood Khan, M. Mahmood Khan, S. Rafiq, L. Cheng, T. Iqbal, M. I. Rasheed, M. Z. Farooq, M. Saeed, N. M. Ahmad, M. B. Khan Niazi, S. Saqib, F. Jamil, A. Mukhtar, and N. Muhammad, *Chem Eng Technol* **43**, 184 (2020).
- [91] Y. Sakamoto, K. Nagata, K. Yogo, and K. Yamada, *Microporous and Mesoporous Materials* **101**, 303 (2007).
- [92] Saif-ur-Rehman, S. Rafiq, N. Muhammad, F. Rehman, M. Irfan, S. U. Zaman, F. Jamil, S. Saqib, A. Mukhtar, K. S. Khoo, M. Mubashir, and P. L. Show, *Fuel* **310**, 122355 (2022).
- [93] J. Shen, M. Zhang, G. Liu, and W. Jin, *RSC Adv* **6**, 54281 (2016).
- [94] S. S. Karim, S. Farrukh, A. Hussain, T. Noor, and M. Younas, *Polymers and Polymer Composites* **29**, S1630 (2021).
- [95] N. F. Himma, A. K. Wardani, N. Prasetya, P. T. P. Aryanti, and I. G. Wenten, *Reviews in Chemical Engineering* **35**, 591 (2019).